Electronic Supplemental Information

Catalytic selective ethane dehydrogenation at low-temperature with low coke formation

Kosuke Watanabe[a], Takuma Higo[a], Hideaki Tsuneki[a], Shun Maeda[b], Kunihide Hashimoto[b] and Yasushi Sekine[*a]

Affiliations: 1: Department of Applied Chemistry, Waseda University, 3-4-1, Okubo, Shinjuku, Tokyo 169-8555, Japan

2: Steel Castings R&D Section, Steel Castings Technology Department,, Kubota Corporation, 1-1-1 Nakamiya-Oike, Hirakata, Osaka 573-8573, Japan

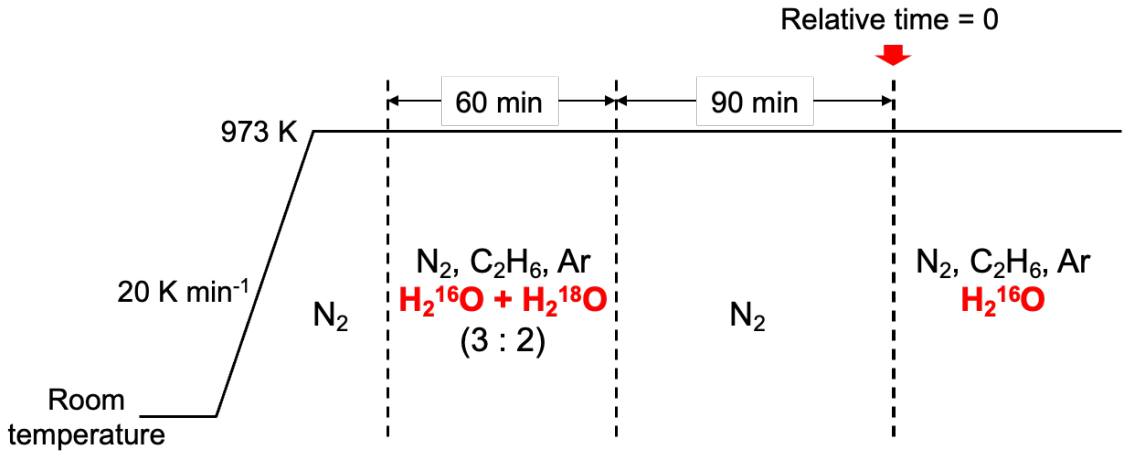

Fig. S1 Measurement protocol of steady-state isotopic transient kinetic analysis with $H_2{}^{18}O$.

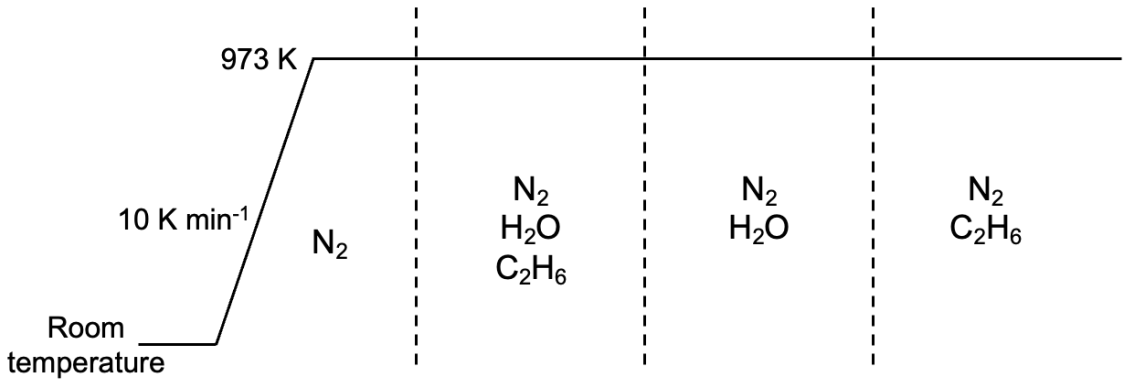

Fig. S2 Measurement protocol of *in situ* Cr *K*-edge XAFS measurement.

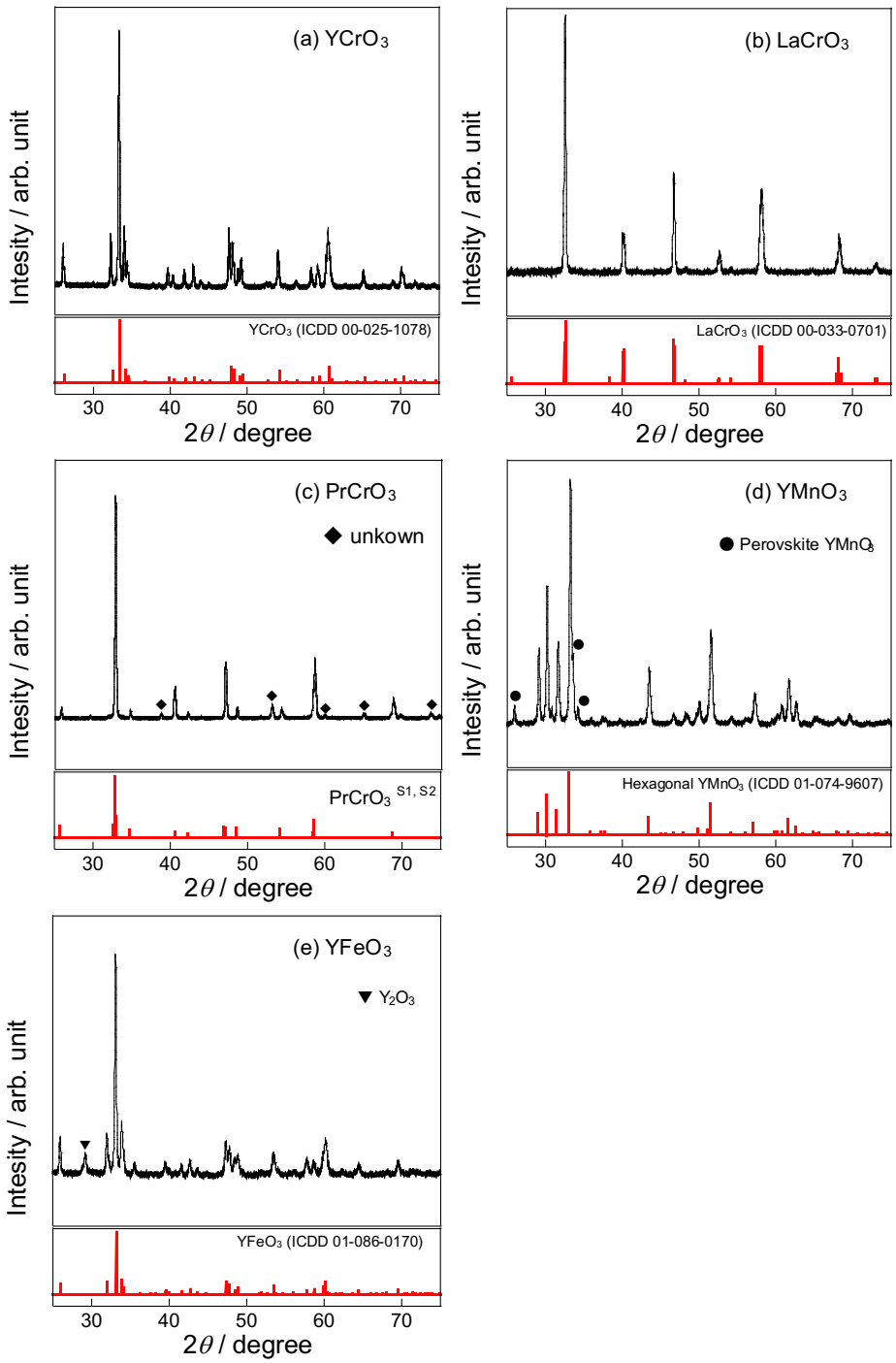

Fig. S3 XRD patterns of fresh $YCrO_3$ (a), $LaCrO_3$ (b), $PrCrO_3$ (c), $YMnO_3$ (d) and $YFeO_3$ (e).

XRD patterns of $YCrO_3$ and $LaCrO_3$ showed no impurity. $YMnO_3$ was a mixture of hexagonal and perovskite phases. On the other hand, $PrCrO_3$ contained unknown impurities and $YFeO_3$ contained Y_2O_3.

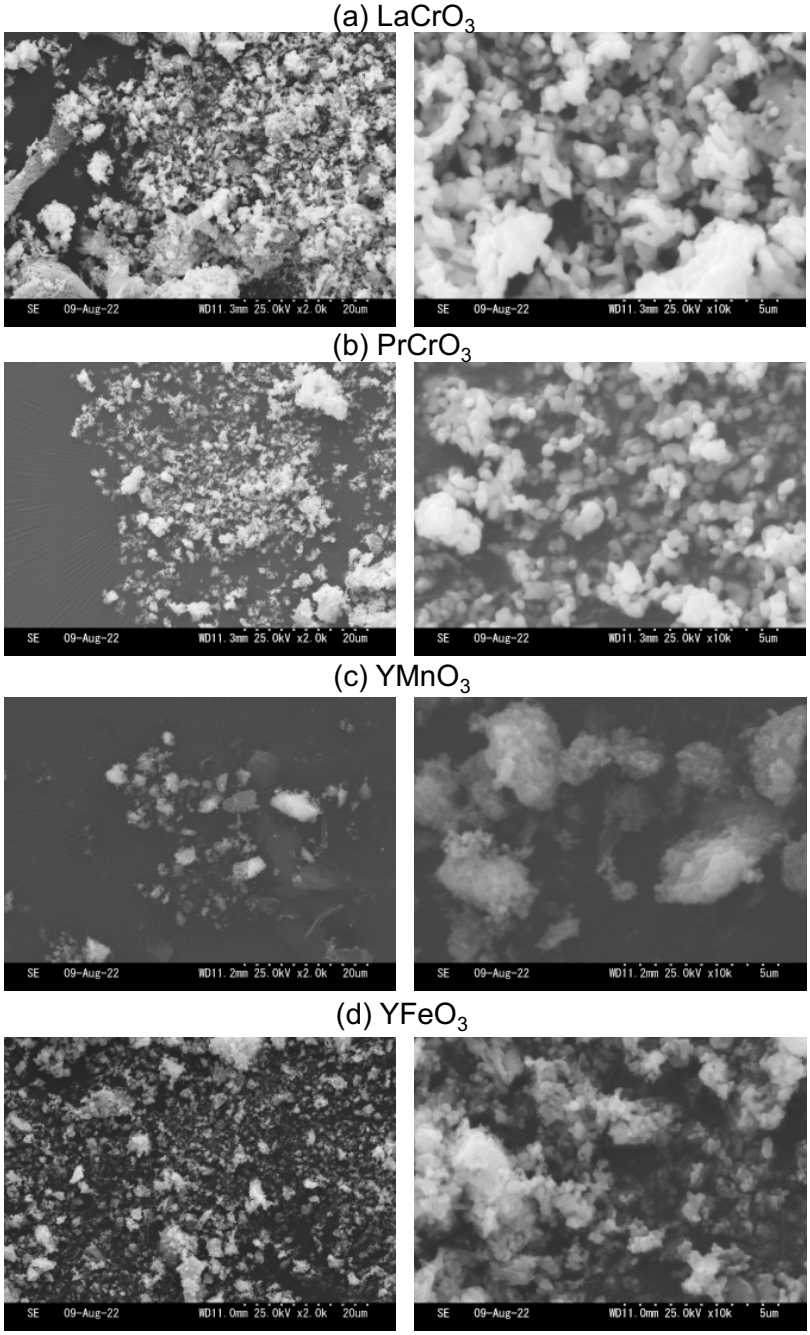

Fig. S4 SEM images for particles of flesh $LaCrO_3$ (a), $PrCrO_3$ (b), $YMnO_3$ (c) and $YFeO_3$ (d).

Figs S4 and S5(a) are SEM images for the particles of the five materials whose catalytic performance was evaluated. For all materials, the micro to sub-micro-sized particles were observed. In particular, Cr-based perovskites and $YFeO_3$ had similar morphology with a smooth surface and rounded corners. On the other hand, $YMnO_3$ appeared to be composed of particles with a relatively rough surface. The specific surface area of these materials (in Table S2) may result from these differences in morphology. However, this tendency toward morphology and ethylene selectivity do

not correlate. Therefore, the surface morphology is considered to be not a critical factor determining the catalytic performance for selective ethylene formation.

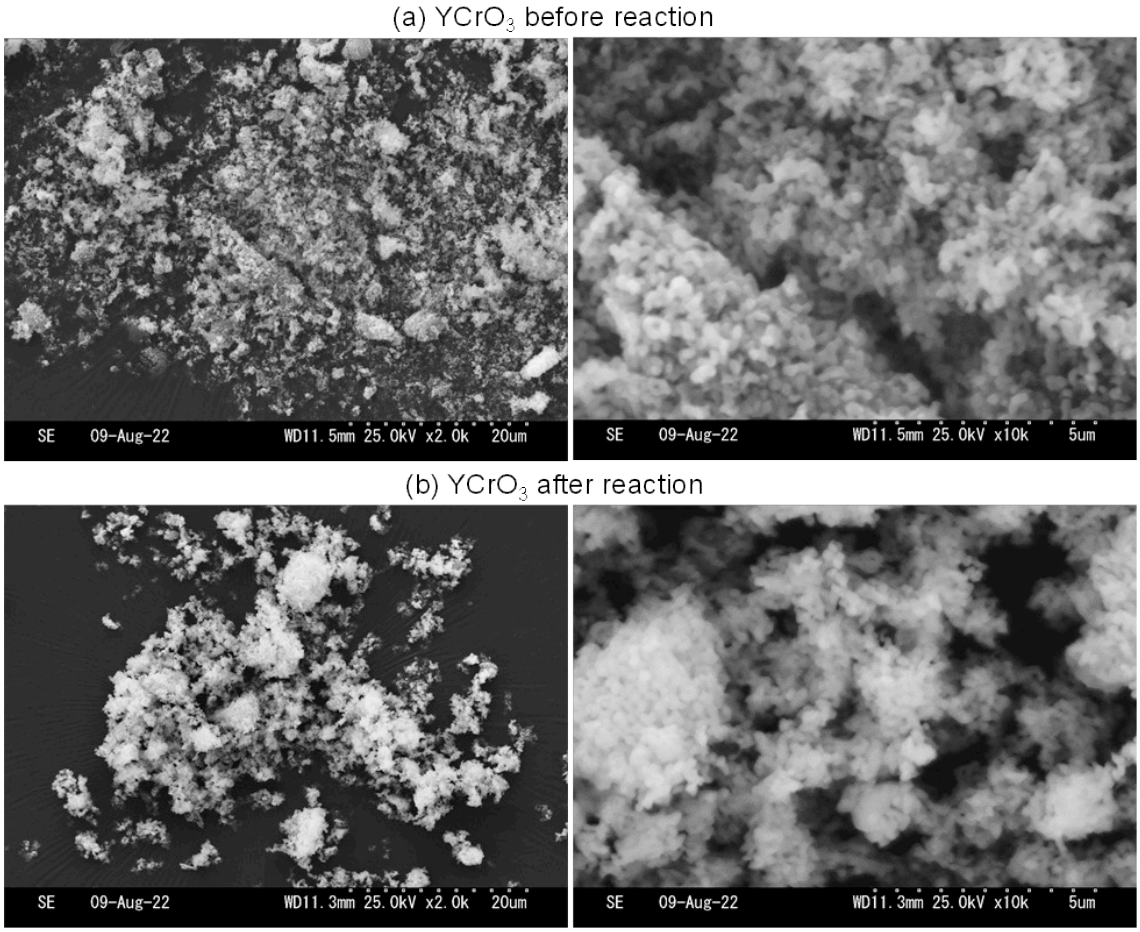

Fig. S5 SEM images for particles of $YCrO_3$ before (a) and after reaction (b).

Figure S5(b) shows the SEM image of $YCrO_3$ after the reaction, which had a very similar morphology to that before the reaction. This indicates that $YCrO_3$ has a stable structure without changing its morphology in the reaction atmosphere.

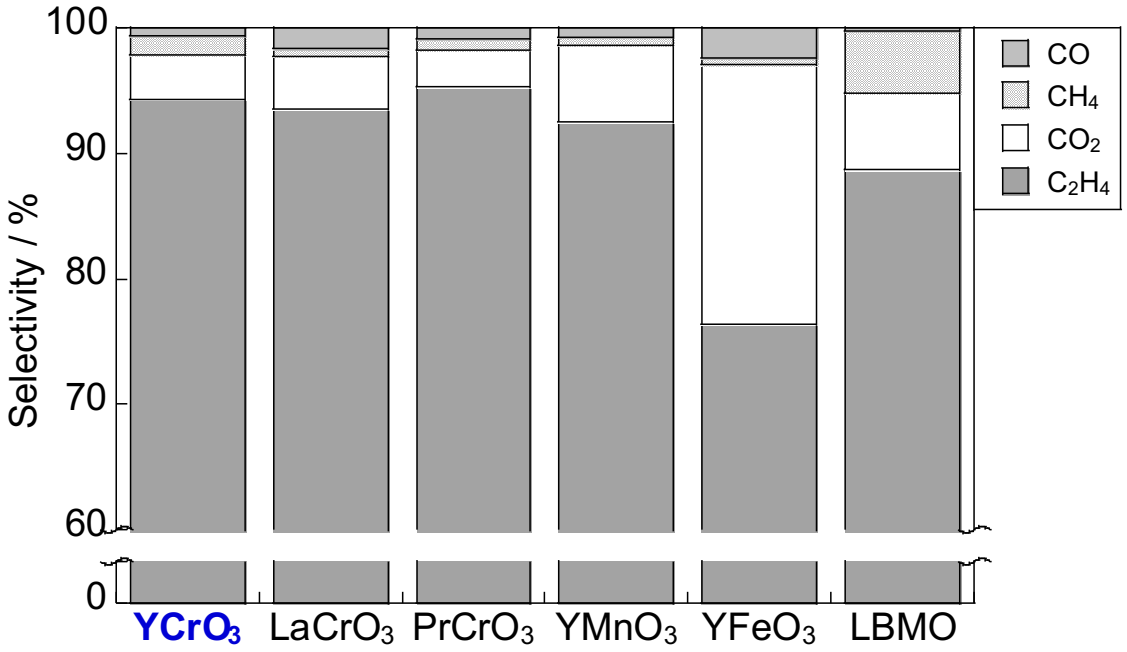

Fig. S6 Carbon selectivity at 973 K over Cr-based, Y-based perovskite and $La_{0.7}Ba_{0.3}MnO_{3-\delta}$ (LBMO).

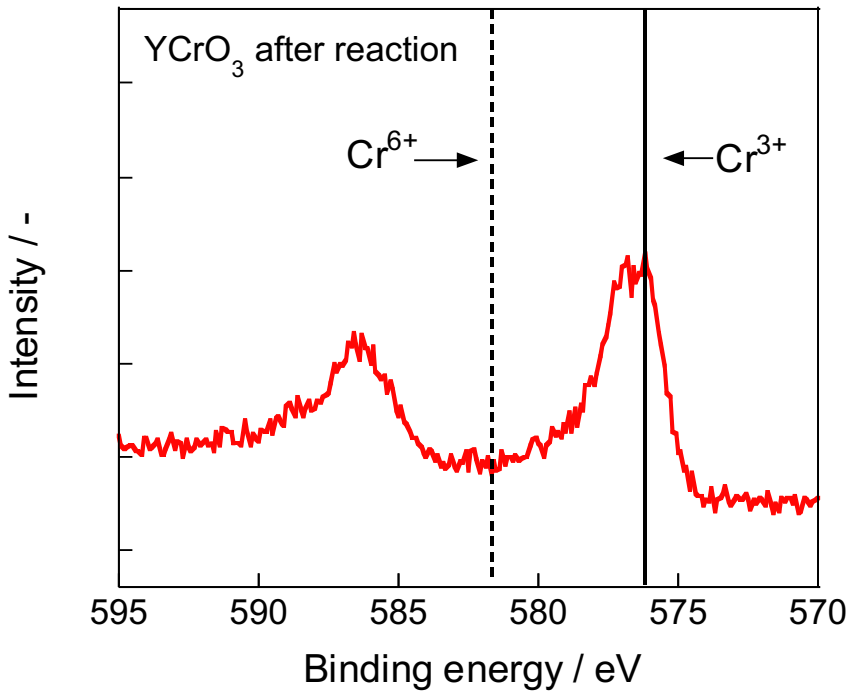

Fig. S7 XP spectrum of Cr2p for $YCrO_3$ after reaction.

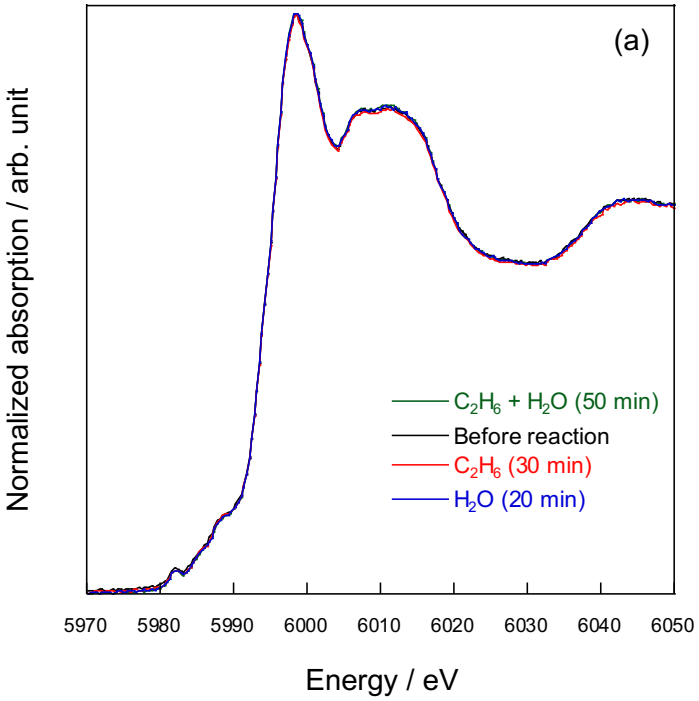

Fig. S8 *In situ* Cr *K*-edge XANES spectra of $YCrO_3$ under wet (green), N_2 (black), dry (red), and H_2O (blue) atmosphere.

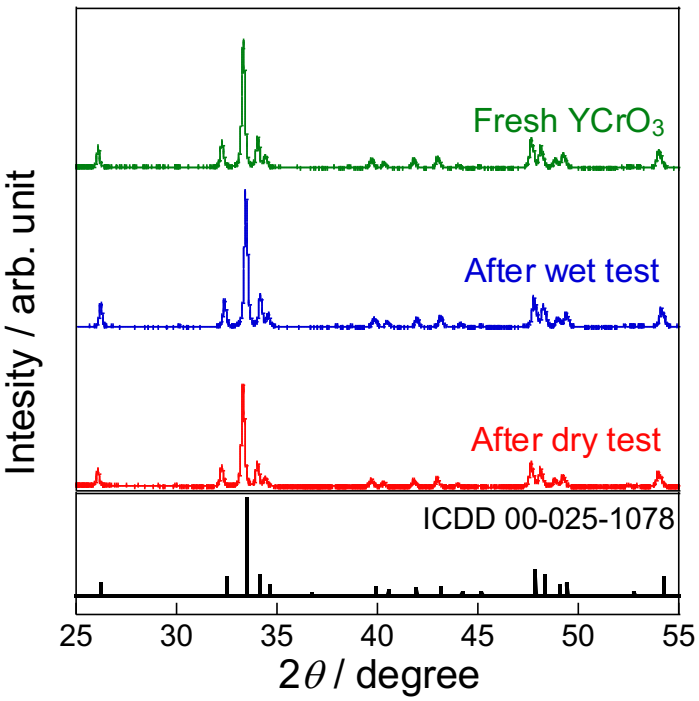

Fig. S9 XRD patterns of fresh and spent $YCrO_3$.

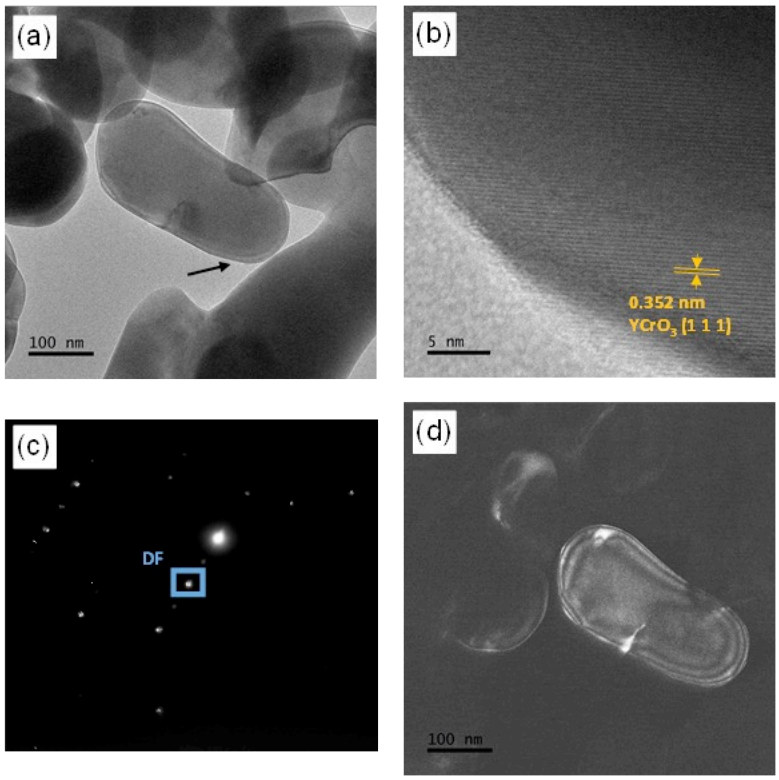

Fig. S10 TEM images (a-b), SAED pattern (c) and dark-field image (d) for particles of flesh $YCrO_3$.

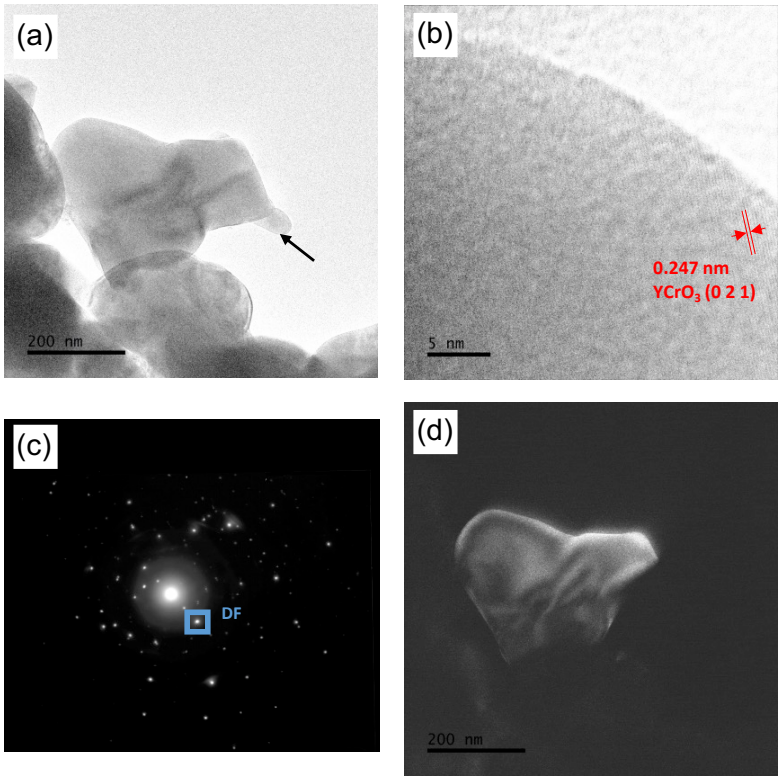

Fig. S11 TEM images (a-b), SAED pattern (c) and dark-field image (d) for particles of $YCrO_3$ after reaction.

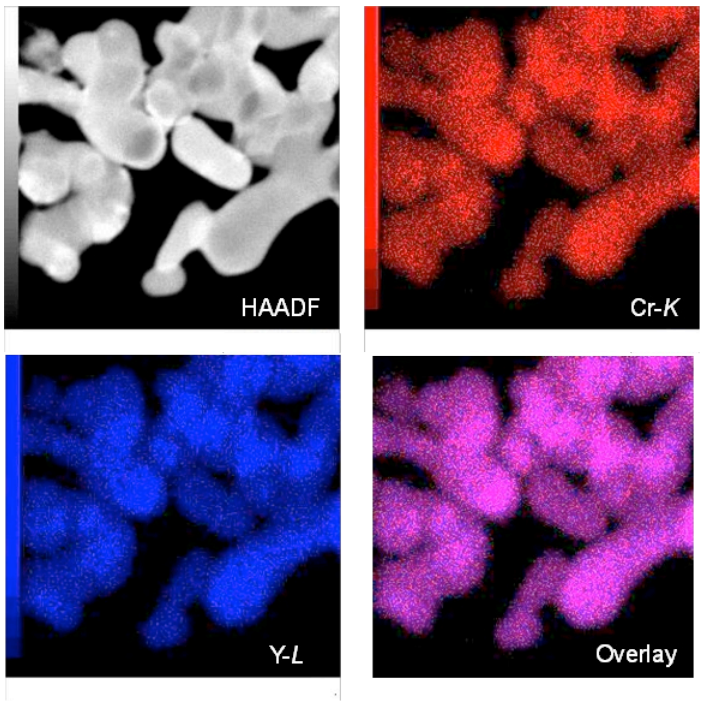

Fig. S12 HAADF and EDS mapping images for flesh $YCrO_3$ (Cr-*K*, red; Y-*L*, blue).

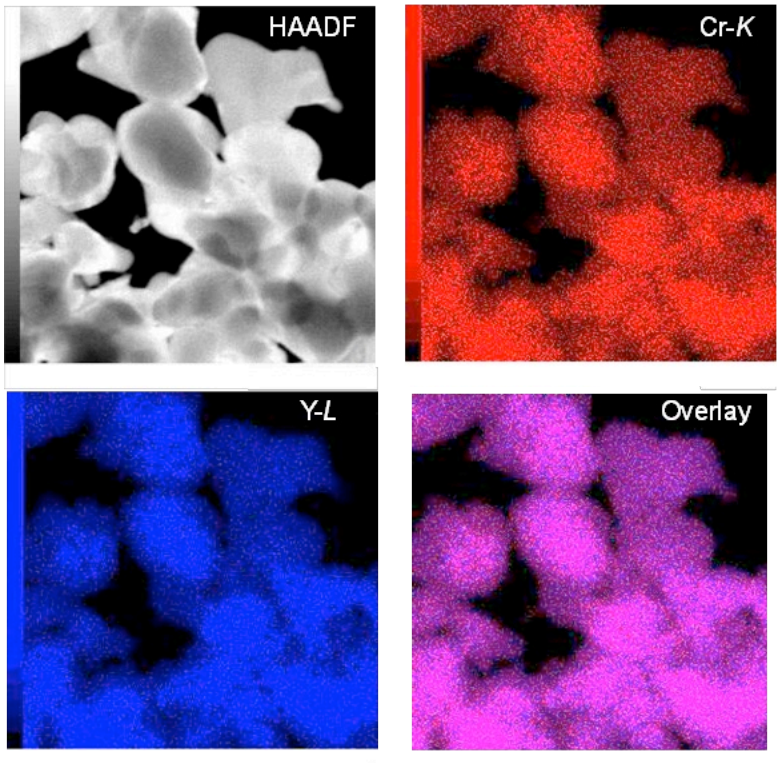

Fig. S13 HAADF and EDS mapping images for $YCrO_3$ after reaction at 973 K (Cr-*K*, red; Y-*L*, blue).

TEM images of particles of $YCrO_3$ before and after reaction are shown in Figs S9(a)-(b) and S10(a)-(b), respectively. The lattice fringes with the spacing of 0.352 and 0.247 nm were considered to correspond to (1 1 1) and (0 2 1) planes of $YCrO_3$ (ICDD 00-025-1078), respectively. Figures S9(c) and S10(c) show the SAED patterns of $YCrO_3$ particles, and the dark field images in Figs S9(d) and S10(d) were obtained using specific spots (in blue squares) in the SAED patterns. These results of TEM including SAED represented that $YCrO_3$ catalyst is the submicron-sized, near-single crystal particle both before and after the reaction. Furthermore, EDS mapping images in Figs S11 and S12 indicated that the catalyst was a single phase $YCrO_3$ particle without segregation of Y and Cr species before and after reaction, which is in accordance with the XRD results. $YCrO_3$ is a stable material whose crystal structure does not change even when exposed to the reaction atmosphere. Therefore, $YCrO_3$ is considered to be a stable coating catalyst that will not delaminate from the tube wall.

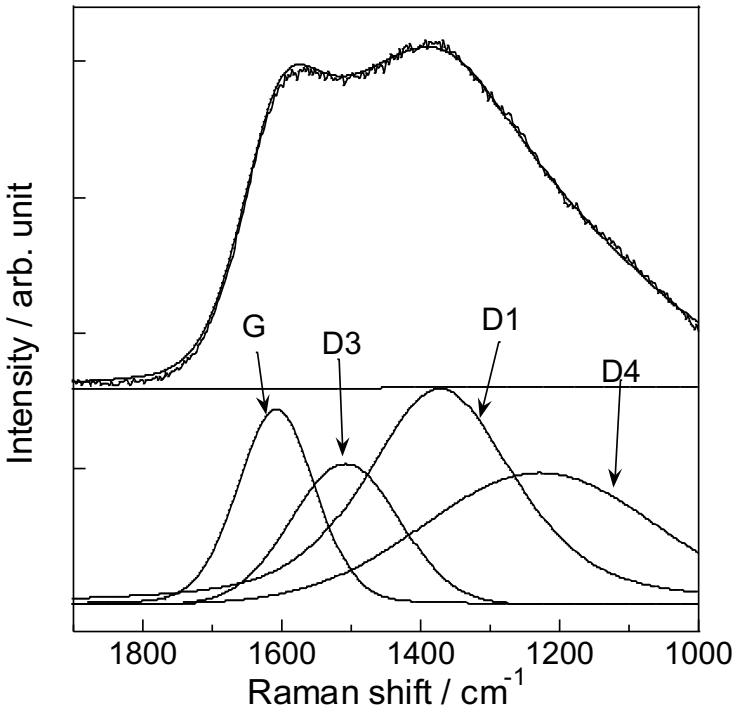

Fig. S14 Deconvoluted Raman spectra of spent $YCrO_3$ after the dry test.

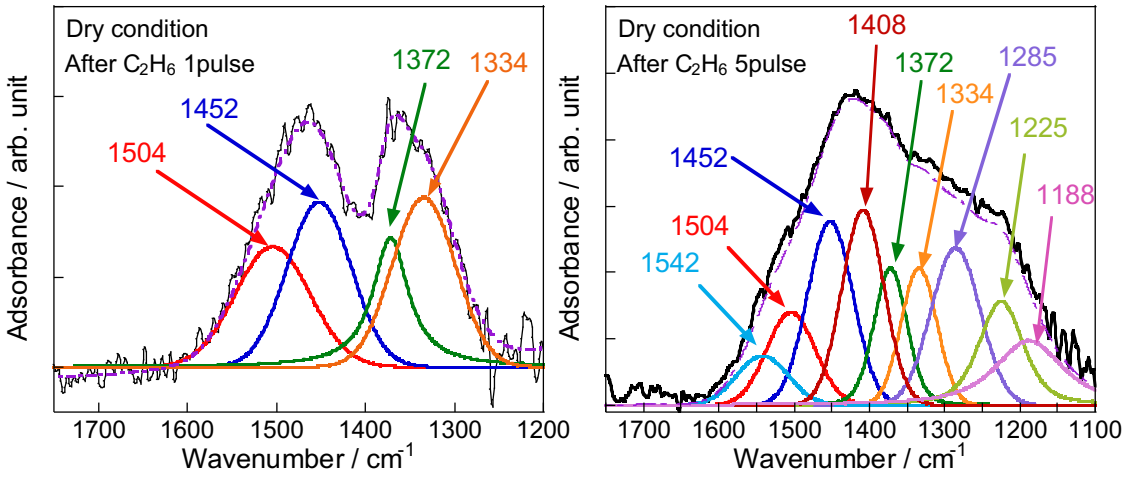

Fig. S15 Deconvoluted IR spectra of observed bands after C_2H_6 pulse under the dry atmosphere.

Table S1 List of chemicals and gases used for catalyst preparation and activity tests.

Chemical	Purity / %
Citric acid monohydrate	99.5
Ethylene glycol	99.5
Lanthanum nitrate hexahydrate	99.99
Praseodymium nitrate hexahydrate	99.95
Yttrium nitrate hexahydrate	99.99
Chromium(III) nitrate nonahydrate	98.0
Iron(III) nitrate nonahydrate	99.0
Manganese(II) nitrate hexahydrate	98.0
Barium nitrate	99.0
C_2H_6 gas	99.5
N_2 gas	99.998
Ar gas	99.995
$H_2{}^{18}O$	98.0 (isotope)

Table S2. Specific surface areas of catalysts and ethylene formation rate per unit surface area.

Catalyst	Specific surface area / $m^2\ g^{-1}$	Ethylene formation rate per unit surface area / mmol $h^{-1}\ m^{-2}$
$YCrO_3$	5.0	3.6
$LaCrO_3$	2.0	2.9
$PrCrO_3$	2.4	4.6
$YMnO_3$	14.0	0.64
$YFeO_3$	2.9	3.2
$La_{0.7}Ba_{0.3}MnO_{3-\delta}$	19.6	0.65

Table S2 portrays specific surface area and ethylene formation rate per unit surface area. Cr-based perovskites ($YCrO_3$, $LaCrO_3$ and $PrCrO_3$) and $YFeO_3$ showed high ethylene formation rate per unit surface area whose order is $PrCrO_3$ > $YCrO_3$ > $YFeO_3$ > $LaCrO_3$. Although $YFeO_3$ shows activity similar to that of $YCrO_3$, it is less selective because it is also more active for sequential oxidation. The activity per unit surface area of $PrCrO_3$ was higher than that of $YCrO_3$, however, since the specific surface area of $PrCrO_3$ is only half that of $YCrO_3$, the activity per weight of catalyst is inferior as shown in Fig. 1. The better performance of $YCrO_3$ is due to the high selectivity for ethylene on the surface of Cr-based perovskites and a relatively high specific surface area among these perovskites.

Table S3 Assignments for curve-fitted bands.

Wavenumber / cm^{-1}	Assignments
1542	C=C stretching (aromatic ring)[23,24] Allylic C-C stretching (C-C=C)[25]
1504	C-C vibration (alkyl aromatics)[26]
1452	-CH, -CH_2 bending (aliphatic hydrocarbon)[25-27]
1408	-CH, -CH_2 bending (aliphatic hydrocarbon)[26,28]
1372	-CH_3 bending (aliphatic hydrocarbon)[25,27]
1334	-CH_3 bending (aliphatic hydrocarbon)[25-27]
1258	-$(CH_2)_n$ - out of plane bending[27]
1225	C-H stretching in aromatic plane[24]
1188	C-H stretching in aromatic plane[24]

References

[S1] Y. Xu, M. Yamazaki, P. Villars, *Jpn. J. Appl. Phys.* 2011, 50, 11RH02.

[S2] S. Geller, *Acta Crystallogr*., 1957, 10, 243–248.